Physical confinement selectively favours bacterial growth based on cell shape

M Sreepadmanabh[1], Meenakshi Ganesh[1,2], Pratibha Sanjenbam[1], Christina Kurzthaler[3], Deepa Agashe[1], and Tapomoy Bhattacharjee[1*]

[1]National Centre for Biological Sciences, Tata Institute of Fundamental Research, Bangalore
[2]Indian Institute of Science Education and Research, Mohali
[3]Max Planck Institute for the Physics of Complex Systems, Dresden
*email: tapa@ncbs.res.in

Abstract

How are bacterial communities altered by changes in their microenvironment? Evidence from homogeneous liquid or flat plate cultures implicates biochemical cues — such as variation in nutrient composition [1,2], response to chemoattractants and toxins [3,4], and inter-species signalling [5,6] — as the primary modes of bacterial interaction with their microenvironment. However, these systems fail to capture the effect of physical confinement on bacteria in their natural habitats. Bacterial niches like the pores of soil, mucus, and infected tissues are disordered microenvironments with material properties defined by their internal pore sizes and shear moduli[7–11]. Here, using three-dimensional matrices that match the viscoelastic properties of gut mucus, we test how altering the physical properties of their microenvironment influences bacterial growth under confinement. We find that low aspect-ratio bacteria form compact, spherical colonies under confinement while high aspect-ratio bacteria push their progenies further outwards to create elongated colonies with a higher surface area, enabling increased access to nutrients. As a result, the population level growth of high aspect-ratio bacteria is more robust to increased physical confinement compared to that of low aspect-ratio bacteria. Thus, our results capture the first experimental evidence that physical constraints play a selective role in bacterial growth based on cell shape.

1. Introduction

Most natural habitats host diverse bacterial communities, which actively perceive and respond to extrinsic environmental cues that reflect the dynamic properties of their microenvironments [7,12]. Identifying the basis of these feedback-response cycles is critical for describing the evolution of natural microbial populations, characterizing host-symbiont crosstalk and interdependency, as well as understanding pathogenesis to design effective antibiotics. A major class of such interactions is understood within the framework of biochemical signalling, where small molecules (such as metabolites, growth factors, antibiotics, and chemoattractants) drive cellular perception and consequent responses [1–4]. These processes also directly impact the composition of natural microbial communities, wherein co-existing species exhibit symbiotic, mutualistic, or predatory interactions with each other [5,6]. However, current experimental approaches designed to explore such interactions rely on bacteria cultured in homogeneous liquid broths or on surfaces of 2D flat plates, which do not capture the structural complexity of their natural niches. Bacteria typically reside in complex and disordered 3D microenvironments like soil, inter-tissue pores, and biological hydrogels such as mucus, which feature a wide range of material properties [9,13,14]. For example, the porosity and stiffness of soil is affected by its moisture content and granularity [15]. The spatial architecture of tissues also undergoes significant structural alterations as a

result of ECM (extracellular matrix) deposition and enzymatic remodelling by fibroblasts and immune cells [16]. Similarly, the viscoelastic properties of mucus vary with diet, inflammatory responses, microbial enzymatic activity, and pathologies like cystic fibrosis [8,17,18] (**Fig. 1a**). Furthermore, bacterial colonies physically constrained within these complex 3D matrices experience diffusion-limited growth [19,20]. In contrast, bacteria growing in homogeneously well-mixed liquid cultures have unrestricted access to nutrients. Similarly, colonies on a flat agar surface are typically exposed to air and receive abundant oxygen supply from the top as well as direct nutrient access from the underlying substratum. Previous work has investigated colony growth under such nutrient-replete 2D conditions while extending growth-generated stresses as a putative mechanism for achieving quasi-3D conformations [21,22]. However, these studies do not fully capture bacterial growth in disordered, confined microenvironments. Growing evidence indicate that bacterial motility is significantly altered by confinement within a granular and porous matrix [23] and the growth of initially smooth, densely-packed bacterial populations under 3D confinement shows generic surface roughening morphodynamics driven by differential nutrient accessibility[20]. Despite this, bacterial population level growth and colony organization under complex and disordered confinement remains insufficiently described. Consequently, how the physical constraints imposed by a 3D growth microenvironment influence microbial populations remains unclear.

In this work, we present the first experimental evidence for confinement-dependent growth dynamics that selectively favour specific bacterial morphologies. We prepare transparent, granular 3D growth media—a special type of porous matrix for direct measurement of bacterial growth as well as visualization of colony organisation under different biomimetic degrees of confinement—that broadly mimic the structural and viscoelastic properties of mucus, a viscoelastic biological hydrogel. Using several different bacterial strains isolated from the gut mucus of red flour beetles we show how an increase in confinement confers a growth advantage to bacteria with a higher aspect ratio. Our study combines quantitative measurements of bacterial growth and colony morphology, agent-based modelling, numerical calculations, as well as *in vitro* co-culture experiments, to establish a generalized principle for growth under confinement. By experimentally manipulating cellular morphology, we also demonstrate a remarkable interconvertible behaviour between high and low aspect ratio forms of the same bacterial species, which strongly implicates single-cell morphology as a generic determinant of colony architecture and growth success under physical confinement. Importantly, we show that population-level variation in growth dynamics can arise without invoking classical adaptive mechanisms such as genetic mutations, behavioural differences, or cellular responses to biochemical cues. Rather, our work establishes that the composition of heterogeneous microbial populations is strongly dependent on efficient colony organization under increased confinement that selectively favours bacterial species with a high aspect ratio morphology. These principles hold immense value towards the experimental elucidation and theoretical modelling of microbial dynamics in complex, spatiotemporally varying natural niches.

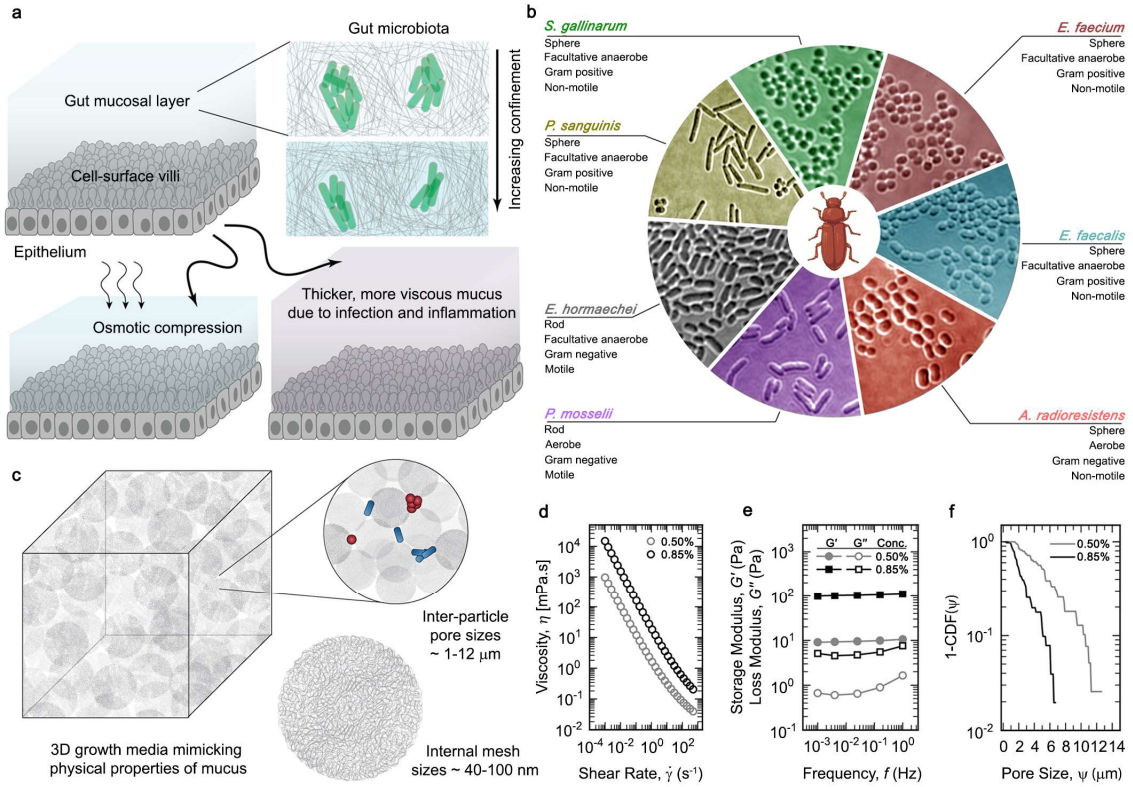

Figure 1: An *in vitro* 3D growth matrix with tunable viscoelastic properties. (a) The physical properties of the mucosal layer are diverse and are altered by factors such as a change in diet, infection, inflammation, and enzymatic degradation of fibers by microbes. (b) Different gut-derived microbial strains from red flour beetles, imaged in brightfield (pseudo-colored for enhanced contrast). (c) By packing highly swollen polymeric hydrogel granules at jamming concentrations, we design an *in vitro* 3D growth medium, which provides a granular and internally porous microenvironment for bacterial growth under confinement. (d-f) The physical properties of the microgel growth medium are highly tunable based on the mass percentage of hydrogel granules relative to liquid LB (%weight/volume). Here, we show both soft and low confinement (0.50%) as well as stiff and high confinement (0.85%) matrices, the viscoelastic properties of which approximately match mucosal samples from natural sources [25]. Rheological measurements shown here either apply a unidirectional shear at different rates to measure the viscosity, or, a small amplitude (1%) of oscillatory strain at different frequencies to measure the shear moduli of the 3D growth media. The storage modulus (*G′*) is a measure of the elastic solid-like nature, while the loss modulus (*G″*) signifies the viscous properties of the material. The porosity of the medium, shown here as a complementary cumulative distribution function (1-CDF) of all the inter-particle pore spaces, determines the degree of confinement, and can be tuned by altering the packing fraction of the hydrogel granules.

2. Results

2.1 Mimicking physical properties of the mucosal microenvironment

To understand how the physical properties of their microenvironment regulate bacterial growth, we avoid the use of laboratory strains to minimize potential experimental artefacts arising from laboratory adaptation, such as mutations accumulated during long-term culture in homogeneous liquid cultures or 2D surfaces. Hence, we isolate several bacterial strains from the gut of the red flour beetle *(Tribolium castaneum*) and identify them using 16S rRNA sequencing. These bacteria naturally reside in a viscoelastic microenvironment, which

ensures minimal interference from culturing practices. Together, these strains include a diverse representation of different envelope properties, metabolic modes, motility patterns, and morphologies (**Fig. 1b**). To create a structural mimic of their natural habitat, we design a jammed microgel-based 3D growth medium that mimics the physical and structural properties of mucus (**Fig. 1b**). Previous structural analysis of mucus indicates different regimes of porosities, spanning from nanometer-scale to micron-scale pores [24]. Further, rheological measurements on mucosal samples from various sources also reveal a broad range of shear moduli (ranging from ~ 1 Pa to ~ 100 Pa) and viscosities (ranging from ~ 10 mPa.s to ~ 5 x 10^5 mPa.s) [25]. By packing micron-scale granules of hydrogels swollen in liquid LB (Luria-Bertani growth medium) beyond their jamming concentration, we manufacture a soft, semisolid 3D matrix with the key physical properties of mucus — especially the porosity (ψ), shear moduli (G' and G''), and viscosity (η) (**Fig. 1d-1f and Supplementary data Fig. 2a**). The nanometer-scale internal mesh sizes of the polymer chains forming each hydrogel granule allows unimpeded uniform diffusion of nutrients and small molecules throughout the bulk medium. The microparticles themselves pack together to generate micron-scale inter-particle pore spaces (ψ), which provide a porous and internally disordered matrix for the bacteria. Within this, bacteria can move by exploring the tortuous pore spaces, as well as achieve 3D colony growth by pushing aside the microparticles to locally and reversibly deform the matrix. Importantly, our 3D microgel growth media retains soft solid-like bulk properties under low shear, while being reversibly fluidizable upon application of shear rates higher than the yield stress limit—which is orders of magnitude lower than the internal turgor pressure of typical bacterial membranes. This allows bacterial colonies to internally rearrange the 3D matrix during growth without altering its material properties, allowing us to reproducibly maintain stable mechanical regimes over long-term culture. Using these platforms, we ask how two different degrees of confinement—representing both extremes of the physical regimes commonly observed for naturally occurring mucus—alter bacterial growth.

2.2 Bacterial growth depends on confinement

The 3D growth medium comprises a low solid fraction, which lends it high optical transparency allowing us to directly visualize bacterial growth under physical confinement. Leveraging this physical property, we homogeneously disperse bacteria in both low confinement and high confinement matrices and employ standard optical density-based absorbance measurements for assaying the temporal change in bacterial biomass (**Fig. 2a**). Optical density measurement (A) in these matrices is linearly proportional to the volumetric density of bacterial cells (λ) as obtained by direct manual counting from micrographs (**Supplementary data Fig. 2b**). Interestingly, we observe a general decrease in the overall biomass production for all bacterial strains with an increase in confinement (**Fig. 2b and Supplementary data Fig. 3**). These effects are not due to compressive deformation of the cell body, since the elastic modulus of the material is orders of magnitude lower than the internal turgor pressure of bacterial cells. We also verify that cellular shape does not get significantly altered under the degrees of physical confinement applied by either matrix (**Supplementary data Fig. 4a)**. To further ensure that an increase in confinement does not cause detrimental effects on cellular physiology, we also culture a genetically modified *Escherichia coli* strain— engineered to visually report both the genome's physical organisation using HU (a DNA-binding protein) tagged to GFP, as well as induction of SulA-driven DNA damage responses — in 3D microgel growth media of both low and high degrees of

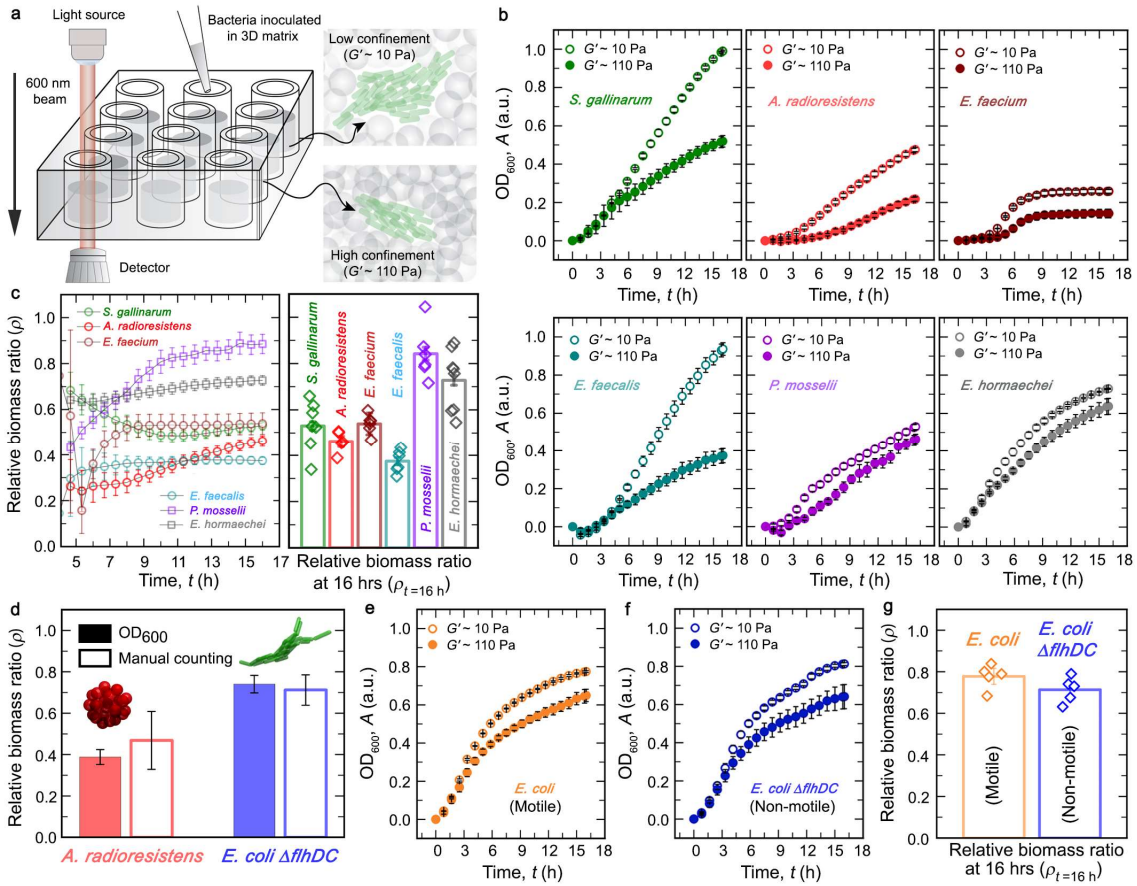

Figure 2: Change in confinement alters bacterial population growth. (a) We use absorbance-based optical density measurements as an indicator of increase in biomass over time to quantify bacterial growth in the 3D microgel media. (b) Representative absorbance-based growth curves over 16 hours indicating confinement-dependent growth dynamics for all bacterial strains (mean +/- s.d., n = 3 technical replicates); *G′* ~10 Pa represents low confinement matrix and *G′* ~ 110 Pa represents high confinement matrix. (c) Relative biomass ratio values for all bacterial strains across all time points, showing that higher confinement demarcates the different microbial species into two distinct sub-groups, indicated by bar graphs representing the plateau value of the relative biomass ratio at 16 hours (mean +/- propagated error, n ≥ 4 biological replicates). (d) Absorbance measurements from 3D growth media mirror the actual microbial load, determined by measuring volumetric bacterial density via manual counting of cells using 3D confocal microscopy (also see Supplementary data fig 2b). Both of these measurements yield comparable relative biomass ratio after 16 hours of growth (mean +/- s.d., n ≥ 3 technical replicates/micrographs). (e-g) Motility does not confer significantly greater fitness benefits under confinement, as tested using a motile and non-motile strain of *E. coli* (the latter carries a deletion in the flagellar protein-encoding gene *flhDC*), which show no significant differences between the growth curves (mean +/- s.d., n = 3 technical replicates) or the relative biomass ratio (mean +/- propagated error, n = 5 biological replicates).

confinement (**Supplementary data Fig. 4b**). We observe that increase in physical confinement neither alters the HU-GFP localization pattern (i.e., no observable change in the genome's spatial arrangement [26]) nor induces SulA expression (indicating DNA damage responses are not triggered [27]). Hence, the decrease in biomass production under higher confinement is likely not due to aberrant cellular physiology leading to loss of cell viability.

To quantify the impact of confinement on growth, we normalize the biomass achieved at each timepoint in the high confinement matrix ($A_{high|16h}$) to that in the low confinement matrix ($A_{low|16h}$) for each strain, which gives the relative biomass ratio (ρ). This parameter initially

varies with time, before achieving a plateau over twelve to sixteen hours for all strains, indicating the existence of a general, non-species-specific effect of confinement on bacterial growth (**Fig. 2c**). To focus on these effects at a stable time point, we quantify the endpoint biomass ratios at the sixteen-hour mark and observe that strains cluster into two well-separated groups—those which perform poorly under increased confinement, and those which remain relatively less perturbed (**Fig. 2c**). For additional rigor, we directly benchmark measurements of endpoint absorbance ratios against volumetric density of bacterial cells as obtained by microscopy and manual counting from the same samples. Importantly, we perform these confirmatory tests for cells possessing two different shapes—approximately spherical and rod-like—thereby establishing the relative biomass ratio (ρ) as a generalised quantitative measure of change in bacterial biomass in 3D matrices (**Fig. 2d**).

A comparison of the various strain-specific morphological attributes listed in Fig. 1G reveals motility and cell body shape as distinguishing features of the two clusters observed in Fig. 2D. Since motility can conceivably allow better dispersion of bacteria in the 3D matrix [23] — thereby improving overall population-level growth through better nutrient accessibility and lesser local crowding—we first test the impact of motility on enhancing growth by employing both a motile (wild-type) and non-motile strain of *E. coli* (harbouring a deletion of a flagella-encoding gene) (**Fig. 2F**). Surprisingly, both strains perform similarly under different degrees of confinement as captured by their relative biomass ratio (ρ) (**Fig. 2e-2g, Supplementary data Fig. 4c and 4d**), invalidating motility as the dominant feature mediating the growth patterns observed under increased confinement. Consequently, we revisit the set of species-specific morphological attributes and note that while all poorly-performing strains comprise low aspect ratio (approximately spherical) cells, the better-performing strains have high aspect ratio cells (rod-like). This observation forces a significant realignment of our perspective on growth under confinement, implicating cellular morphology as the attribute critical to growth success under spatial constraints.

2.3 Single-cell morphology dictates colony shape

Unlike growth on homogeneous 2D interfaces or in well-mixed liquid media, growth under physical confinement imposes spatial constraints and consequent nutrient limitations on bacterial colonies. To determine how different single-cell morphologies affect colony architecture, we employ an agent-based simulation using the CellModeller platform [28], maintaining all growth parameters constant and only altering the cellular aspect ratio. We simulate growth undertaken by low aspect ratio (approximately spherical) and high aspect ratio (rod-shaped) cells (**Fig. 3a and Supplementary data movie 1**). While most high aspect ratio bacilli (rod-shaped) cells such as *E. coli* exhibit cell division patterns that produces progeny cells oriented along the parental cell's longitudinal axis, several low aspect ratio coccoid (spherical) species show planes of division that are either randomly or perpendicularly positioned to previous division planes, which allow a higher degree of freedom for the orientation of progeny cells following division [29]. We incorporate these patterns in our simulations by implementing that high aspect ratio bacteria divide and produce progeny oriented along the length of the parent cell, whereas low aspect ratio cells produce progeny oriented along a randomly chosen direction. Under these conditions, striking differences emerge, wherein the high aspect ratio bacteria generate elongated colonies, while the low aspect ratio bacteria give rise to rounded 3D colonies. We further characterise these using a

parameter termed the shape factor (ϕ), defined as the ratio between the perimeter and square root of area for the projection of a given colony. A low value for the shape factor (ϕ) indicates that the colony has a relatively lower exposed surface area as opposed to the enclosed volume. We find that the low aspect ratio bacteria predominantly organise into colonies with a low shape factor, and the high aspect ratio bacteria form elongated, high shape factor colonies (**Fig. 3a**). Hence, single cell morphology appears to strongly dictate overall colony architecture.

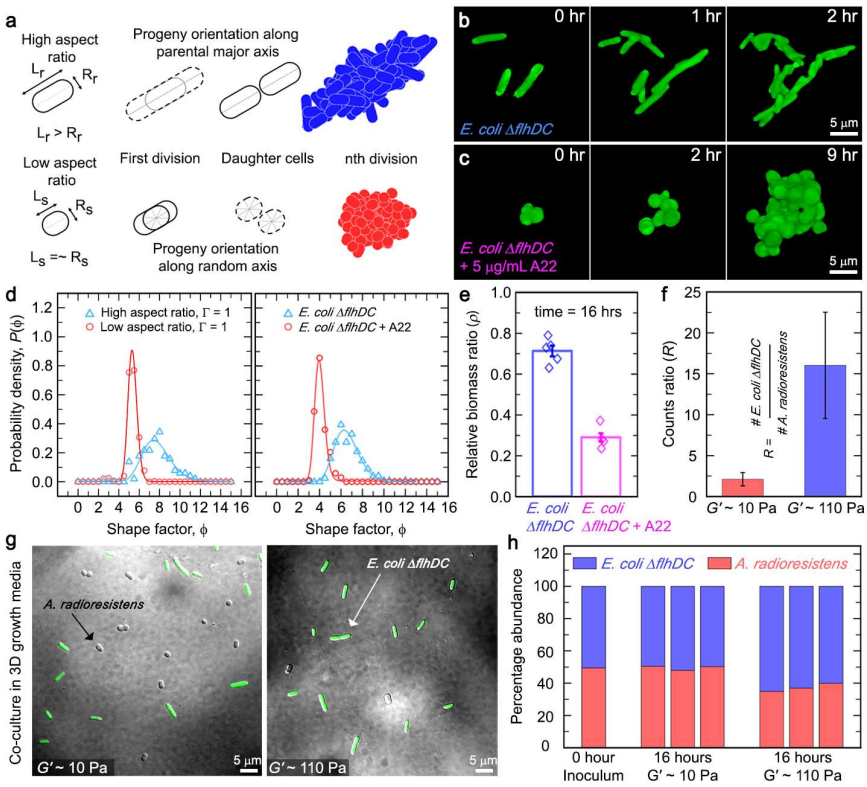

Figure 3: Bacterial morphology determines colony architecture and competitive outcomes. (a) We perform agent-based simulation of 3D colony growth for both high and low aspect ratio cells. In these simulations, progeny of high aspect ratio cells exhibits a directional bias along the parental axis, whereas those of low aspect ratio cells are more flexible grow along any random axis. (b) Rod-shaped high aspect ratio *E. coli* cells give rise to elongated colonies under confinement as they proliferate by pushing their progeny outwards. (c) Treatment with 5 μg/mL of the MreB perturbing compound A22 produces approximately spherical *E. coli* cells, which result in a rounded colony architecture. Micrographs in both (b) and (c) are generated by capturing the front view of a 3D volumetric projection. (d) Quantitative analysis of colony morphology using the shape factor (ratio between perimeter and square root of the area obtained from 2D projections of colonies) shows a significant difference between high and low aspect ratio cells, for both computational simulations ($n \geq 200$, from 10 simulations) and experiments ($n \geq 200$). (e) Relative biomass ratios for rod-shaped and spherical *E. coli* indicate that rod-shaped cells are less affected than spherical ones under increased confinement, i.e., have ρ values closer to 1 (mean +/- propagated error, $n \geq 4$ biological replicates). (f and g) Direct visualization and endpoint counting of cells from 3D co-culture assays including both low aspect ratio (*A. radioresistens*) and high aspect ratio (non-motile *E. coli*) cells show that the latter enjoys a superior growth advantage under increased confinement, at the expense of the former (mean +/- s.d., n = 3 biological replicates). (h) Analysis of genomic DNA extracts pooled from similar 3D co-culture setups confirm that high aspect ratio bacteria are more robust to increase in physical confinement compared to low aspect ratio cells (n = 3 biological replicates).

We experimentally test this by live imaging the 3D colony growth of non-motile rod-shaped *E. coli* under high confinement matrices and observe patterns consistent with our

computational model. Rod-shaped *E. coli* cells undertake volumetric growth along the parental axis, and push their progeny cells outward, leading to elongated colony architecture (**Fig. 3b, Supplementary data Fig. 5a, and Supplementary data movie 2**). Next, we directly alter the morphology of non-motile *E. coli* using sub-MIC dosages of the MreB-perturbing compound A22 [30]. Sub-lethal concentrations (5 μg/ml) of the drug induce aberrant division, rendering the rod-shaped *E. coli* into spherical cells. Again, as predicted by our computational model, the A22-treated low aspect ratio cells assume a rounded colony morphology (**Fig. 3c, Supplementary data Fig. 5b, and Supplementary data movie 2**). By quantitatively analysing the shape factor (ϕ) of the max projected fluorescent micrographs of colonies formed by rod-shaped and spherical cells, we find both the experimental and computational data to be in good agreement, with the single cell morphology being strongly implicated as the key determinant of colony-level organisation under 3D growth conditions (**Fig. 3d, Supplementary data Fig. 5c and 5d**).

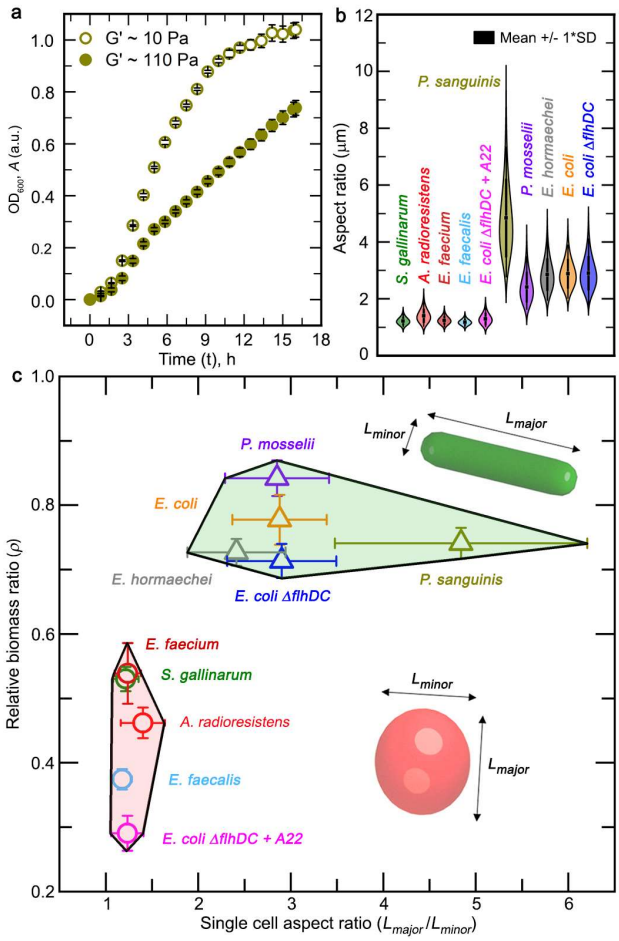

Figure 2: Single cell morphology enables physical confinement to selectively favour elongated colony architecture (a) Growth assays indicate that *P. sanguinis* performs at par with rod-shaped bacteria across two different degrees of confinement (mean +/- s.d., n = 3 technical replicates. (b) Manual measurements of the aspect ratios of bacterial cell bodies for all ten strains used in this study, measured from samples in the late exponential phase (n ≥ 80). (c) Microbial growth under confinement, as described using a phase space defined by the relative change in biomass production under increased confinement (the relative biomass ratio) vs. single cell morphology (mean +/- propagated error).

2.4 Confinement selectively favours rod-shaped cells

A comparison of the relative biomass ratio (ρ) for rod-shaped and spherical *E. coli* reveals that alteration in shape severely compromises growth success under increased confinement, mirroring the trends exhibited by high and low aspect ratio gut-derived bacteria (**Fig. 3e, Supplementary data Fig. 5e and 5f**). In fact, the relative biomass ratio of the spherical *E. coli* is quite similar to that of the naturally low aspect ratio cells ($\rho \leq 0.5$). Together, these observations highlight how cellular morphology enforces differences in the colony architecture of rod-shaped and spherical cells during growth under confinement. We further find that these trends depend only on the cellular shape rather than other environmental variables. More specifically, we alter the nutrient composition for the 3D matrices from LB broth to minimal media (M9) supplemented with glucose and amino acids (**Supplementary data Fig. 6a and 6b**). When cultured in the minimal media matrices, high aspect ratio *E. coli* and low aspect ratio *A. radioresistens*

mirror the relative biomass ratio trends observed in LB-based matrices, indicating that the relative biomass ratio patterns are independent of nutrient profile (**Supplementary data Fig. 6c-6e**). The above results lead to the prediction that all else being equal, rod-shaped bacteria should have a growth advantage over spherical bacteria under higher confinement. We additionally verify this using numerical calculations of bacterial colony growth, wherein we consider two different colony architectures—ellipsoidal and spherical—formed by high aspect ratio rod-shaped bacteria and low aspect ratio spherical bacteria, respectively. Factoring in the previously established limits on effective nutrient diffusion inside a 3D bacterial colony up till a depth of 10 μm from the surface [20]—which sets a limit on the actively proliferating fraction of a given 3D bacterial colony—we estimate the proportion of actively growing bacterial cells in colonies of either geometry with different sizes (**Supplementary data Fig. 5g and 5h**). Ellipsoidal colonies comprising of rod-shaped cells retain a higher proportion of cells in the actively growing zone as opposed to spherical colonies of comparable sizes. Together, the above results indicate that high aspect ratio bacteria produce elongated colonies, which allow better nutrient access in a 3D matrix, thereby enabling superior growth under increased confinement.

To test whether this effect provides a competitive advantage to high aspect ratio cells in a mixed population, we carry out co-culture assays that combine both high aspect ratio and low aspect ratio cells across two different degrees of confinement (**Fig. 3f-3h, Supplementary data Fig. 7a and 7b**). For this, we prepare an inoculum with equal parts of both high aspect ratio cells (non-motile *E. coli*) and low aspect ratio cells (either *A. radioresistens* or *E. faecalis*), that we homogeneously disperse in both low and high confinement 3D growth matrices. Following sixteen hours of growth, we manually tally the number density of each type of bacteria using microscopy to obtain the number of cells per unit volume of sample. We observe that as expected, high aspect ratio bacteria outperform their low aspect ratio counterparts; and importantly, this effect is stronger under higher confinement. Parallelly, we also perform bulk genomic DNA extraction and quantify the relative abundance of specific marker genes unique to each strain. Our bulk genomic analysis mirrors the trends observed with manual tallying of the number density: despite identical nutrient media, under low confinement, relative strain abundances are similar to proportions in the starting inoculum, whereas, under high confinement, rod-shaped bacteria gain a substantial advantage. These results thus validate high aspect ratio morphology as a beneficial attribute under spatially confined growth.

In nature, cells exhibit morphological alterations under specific environmental conditions. For instance, uropathogenic *E. coli* transition between coccoid and rod-like morphologies during infection progression [31]. Such shape changes might confer growth advantages in porous 3D environments such as tissues. We test this hypothesis using *P. sanguinis*, a strain that shows both spherical and rod-shaped morphology—similar to previous reports on *P. denitrificans*—but exhibits growth in an elongated rod-like fashion under confinement [32,33] (**Fig. 4a, Supplementary data Fig. 7c, and 7d**). We assay the growth of *P. sanguinis* across two different degrees of confinement and find that it mimics the relative biomass ratio trend observed for high aspect ratio bacteria. This further validates that the elongated colony structure of high aspect ratio strains confers a relative advantage under increased degrees of confinement.

Thus, we conclude that the aspect ratio of individual cells is a key determinant of the relative biomass ratio under 3D confined growth. To test this, we measure the cell body

morphology of all the different bacterial strains used in our experiments and plot their individual aspect ratio by measuring the major axis and minor axis of the cell body. Distribution of these aspect ratios captures two different populations, separated by their morphology (**Fig. 4b**). Superimposing this with our previous results on the relative growth ratios across two different degrees of confinement, we observe a remarkable compartmentalization of the different bacterial strains into two non-overlapping domains. This phase space—defined by the single-cell morphology and consequent growth performance under elevated confinement—underscores the idea that with an increase in confinement, single-cell morphology is the primary determinant of growth success in complex environments (**Fig. 4c**). Effectively, we demonstrate that the selective pressure exerted by the physical microenvironment in terms of confinement-induced spatial constraints strongly favours high aspect ratio cellular morphology due to its efficient colony organisation.

3. Discussion

Our work provides the first experimental evidence implying that physical confinement can play a selective role in deciding bacterial growth fitness within their natural niches. High aspect ratio bacteria leverage growth anisotropy to form elongated colonies with higher surface area, allowing better nutrient accessibility as opposed to the spherical colonies formed by low aspect ratio bacteria. Increased confinement strongly selects high aspect ratio cells for more efficient growth — a trend that holds even for high and low aspect ratio forms of the same bacterial strain, indicating a remarkable interconvertible behaviour governed solely by cellular shape. Importantly, we demonstrate the potential to use such constraints to alter bacterial community composition under biomimetic mechanical regimes. Thus, our results represent a paradigm shift in how we conceptualize bacterial growth within complex natural habitats.

In microbial ecology, the present mechanistic understanding of predator-prey interactions, niche partitioning, and community organization largely relies on a framework comprising genetic mutations, behavioural patterns, and biochemical signalling [34–38]. Notably, our platform does not preclude such chemical interactions due to its porous and permeable nature. This presents an opportunity to capture the dynamics of a chemical signalling landscape coupled with different mechanical regimes, enabling a more comprehensive experimental recapitulation of natural niches. While the permeable nature of our 3D matrix allows unimpeded small molecule diffusion, several biological niches such as soil and aquifers resemble semi-permeable porous media with non-deformable, rigid physical barriers. We expect that the reduced nutrient availability and severe spatial restrictions in such contexts significantly restrict colony growth and organization. Recreating such regimes *in vitro* will require the development of semi-permeable 3D scaffolds. Further, within the temporal window for our assays, we do not observe significant contributions from either aberrant phenotypes or perturbed physiologies. However, environmental pressures in the form of nutrient deprivation, high mechanical stiffness, and antagonistic interspecies interactions are known to induce the expression of stress genes, alter metabolism, trigger extreme phenotypes (such as filamentous growth), and favour mutational biases [39–44]. Such factors are likely to affect long-term bacterial growth— hence, future work that investigates bacteria under similar conditions over extended durations could provide interesting insights into the long-term effects of confinement on bacterial communities. Presumably, our system can be engineered to recreate

such effects by altering the nutrient media composition and tuning the mechanical stiffness of the matrix. We speculate that such environmental constraints will selectively favour a subset of adaptive mutations with the potential to alter evolutionary trajectories.

Current descriptions invoke either genetic mutations or biochemical signalling as the primary mechanisms via which bacteria perceive and respond to their microenvironment. By contrast, we argue that the spatial constraints imposed by their microenvironment exert a more general effect, irrespective of specific organismal biology. Our conceptual framework can be employed to generate coarse-grained predictions of population dynamics under different biophysical regimes. Understanding how bacteria grow in complex, disordered 3D environments such as tissues, mucus, and soil, is also central for combating antibiotic resistance, improving agricultural practices, and bioremediation — underscoring the high-value practical applications of our work.

4. Methods

4.1 Preparation and Characterization of 3D growth media

We prepare the 3D matrices by dispersing dry hydrogel granules of Carbopol C-980 (Lubrizol) at either a 0.50% or 0.85% (w/v%) concentration in 2% (w/v %) liquid LB (Sigma, LB Lennox) media. While preparing minimal media matrices, we replace LB media with M9 media (BD Difco, M9 Minimal Salts) supplemented with 0.2% glucose and 0.2% milk protein hydrolysate as a source of amino acids. The hydrogel suspension is vigorously stirred for at least 2 hours to ensure complete hydration of the dry granules. Since the Carbopol C-980 is a negatively charged hydrogel, we neutralize the pH of this suspension to 7.4 using 10N NaOH. At pH 7.4 the hydrogel granules or microgels swell maximally to an extent when individual granules jam against each other forming a transparent and disordered solid matrix. We determine the viscoelastic properties of jammed microgels using oscillatory shear rheology on a shear-controlled Anton Parr (MCR302e) rheometer with a roughened cone-plate measuring tool. We adjust the solid fraction of 3D growth media to achieve an elastic storage modulus range between 10 Pa to 110 Pa, that spans the measured range of biological mucosal samples. To measure the yield stresses and viscosity of the hydrogels, we apply unidirectional shear at varying rates while recording the shear stress response. As shown in Fig. 1, our microgels behave as yield stress materials, which are reversibly fluidizable upon application of the threshold shear rate but retain a soft solid-like nature below this regime. To characterize the internally porous nature of these gels, we track the thermal diffusion of 200 nm-sized fluorescent tracer beads within the inter-particle pore spaces and acquire images within time intervals of 17 ms with the 40X objective of an inverted point-scanning laser confocal microscope (Nikon A1R HD25). Individual beads are tracked with sub-pixel precision using a custom-written MATLAB script based on the Crocker-Grier algorithm [45], and the mean-square displacement (MSD) is quantified as a function of lag time. Over short time scales, the beads diffuse unimpeded, with the MSD increasing linearly with time, followed by a plateauing at longer time scales once they become constrained by the pore boundaries. A sum of the square root of these plateau values and the bead diameter yields the dimensions for the smallest confining pore space.

4.2 Isolation, *in vitro* culture, and characterization of bacterial strains

We isolate seven different microbial species from red flour beetles (*Tribolium castaneum*) and identify these by Sanger sequencing of the 16S rRNA gene using the

universal 16S primers 27F (5'-AGAGTTTGATCCTGGCTCAG-3'), and 1492R (5'-GGTTACCTTGTTACGACTT-3'). Following the alignment of both forward and reverse sequences, a homology search using NCBI BLAST is carried out to identify the closest bacterial species for each such amplicon (16S sequences provided for each isolate in **Supplementary information**). Primary isolates from these are cultured in 2% LB broth and cryopreserved as glycerol stocks (20% v/v). For each experiment, a shaken culture of 1% stock dilution in LB broth is grown at 30ºC for ~20 hours to achieve a stationary phase culture. From this, a 1% inoculum is added to fresh 3D growth media and homogeneously dispersed by gentle pipette mixing. To promote better growth in the case of *E. faecalis* and *E. faecium*, overnight cultures are directly set using 3D hydrogel media. We also employ two strains of *E. coli* – one, the wild-type motile strain, and the second carrying a deletion in the flagellar gene flhDC, that renders it non-motile. For antibiotic treatment of *E. coli* with A22, we maintain a sub-MIC concentration of 1 μg/ml in LB and 5 μg/ml in 3D media. To characterize the bacterial morphology, we dilute samples using either LB or 0.5% 3D growth media and spread these on a flat agar pad (1% (w/v) agar in water), placed inverted onto a glass bottom dish. Images are acquired using a point-scanning laser confocal microscope. We ascertain the suitability of LB broth as a nutrient medium for all bacterial strains by assaying their growth in shaken liquid cultures (**Supplementary data Fig. 1**). To measure the cellular morphology, we manually segment micrographs in ImageJ and use in-built functions to quantify the cell body area and aspect ratio. To test for genomic DNA damage-triggered responses, we use *E. coli* strains carrying a constitutively-expressing GFP-tagged histone protein (HU-GFP) that marks the DNA, along with an mCherry-tagged DNA damage response-triggered protein (SulA-mCherry). These are cultured for 24 hours in microgels of different stiffnesses and imaged using a confocal microscope. As an additional control, we induce DNA damage in an exponential-phase culture of bacterial cells cultured in liquid LB by treating with 5 μg/ml of the DNA damage-inducing drug MMC, which exhibits strong SulA-mCherry expression.

4.3 Growth assays

We assay microbial growth in 3D growth media using absorbance-based optical density measurements at 600 nm. Samples prepared as described above are dispensed as 200 μl replicates into 96-well plates, and readings are acquired at 10-minute intervals for 16 hours using a multi-mode plate reader (Varioskan Lux) with temperature control (set to 30ºC). All data are normalized by subtracting the initial timepoint value (except for antibiotic-treated samples, where we normalize using the lowest absorbance value to account for initial cell death). This gives a measure of the net increase in biomass over time. For 3D co-culture assays, all parameters are maintained identical to the above, except the initial inoculum, wherein both competing strains are added in similar proportions by normalizing the optical density of overnight-grown cultures. To maintain identical culturing conditions as followed for the individual growth assays, we dispense these samples in a 96-well plate and grow them for 16 hours at 30ºC. Following this, we pool together all the technical replicates for each gel type and homogeneously mix the sample. From this, a 20 μl aliquot is used for manual bacterial counting, with the rest being processed for genomic DNA extraction (described below).

4.4. Manual counting of single cells from micrographs

Briefly, we set up growth curve assays for the non-motile *E. coli ΔflhDC*, as described above, in multiple triplicate sets, for both low confinement and high confinement matrices. At specific time points separated by three-hour intervals, we obtain an optical density

measurement for each set. Each individual replicate belonging to this set is harvested, and diluted using LB. We scale the dilution factor for each timepoint following the first one to achieve approximately the same final density of bacterial cells. These samples are then mixed with microgel (to prevent cells from settling during the counting procedure) in a 1:1 ratio, following which 200 μl of this sample is dispensed into a glass-bottomed 35 mm dish and fixed 3D volumes from each are imaged using a confocal microscope. The total number of bacteria is tallied using automated thresholding and segmentation functions available in ImageJ, as well as the 3D Cell Counter plugin. Using this, we calculate the number of bacteria per mL from the original sample and plot this against the measured absorbance value. We observe a roughly linear relation between the manually counted number of cells and the optical density of the sample, confirming that absorbance values provide an accurate estimate of the total bacterial biomass in 3D growth media.

To verify this for the relative biomass ratio metric, we set up growth curve assays for both *A. radioresistens* and the non-motile *E. coli ΔflhDC*, as described above, in both low and high confinement matrices. Immediately after the growth curve assay concludes, we pool together all replicate samples of each bacterial strain and each specific confinement type in separate microcentrifuge tubes. This is well-mixed to ensure homogeneous dispersion of the bacteria. 20 μl of this is added to 1 ml of 0.50% microgel (to prevent cells from settling during the counting procedure) and mixed thoroughly to break up the colonies into single cells. 200 μl of this sample is dispensed into a glass-bottomed 35 mm dish and imaged using a confocal microscope. From the images, individual bacteria are manually identified and tallied. We then compare the ratio of endpoint absorbances from 0.85% microgel to 0.50% microgel for both bacterial strains with the ratio of numbers obtained by manual counting for identical samples.

For the co-culture experiments from section 4.3, we mix the 20 μl of pooled specimen sample in 1 ml of 0.50% microgel and vigorously mix the same to break up all colonies into individual cells. These are spread on flat agar pads as described above and imaged using confocal microscopy. From the images, individual bacteria are manually counted and tallied for each field, giving us a ratio of bacterial counts obtained between 0.50% and 0.85% gels for each individual strain.

4.5. Colony morphology experiments

For live-cell imaging of bacterial colonies, we use 35 mm plastic dishes with a central circular cavity (15 mm in diameter) sealed off with a glass coverslip for optimal quality imaging. Samples for assessing the colony morphology are prepared exactly as described above for the growth curve experiments. 200 μl of well-mixed samples are dispensed into the glass-bottomed cavity of these dishes. Using a sterile coverslip, we scrape the top of this sample to ensure a smooth, flat layer. To prevent evaporative losses, we gently layer the top of the sample with 1.5 ml of mineral oil (Sigma). This oil is permeable to gases; hence the microgel-suspended bacteria are not cut off from oxygen supply. Plates prepared in this manner are placed in an incubator maintained at 30ºC for 16 hours. Following this, we acquire z-stack images of the bacterial colonies using confocal microscopy. Colony morphology is analysed by either manually or automatically segmenting 2D projections of the individual bacterial colonies, followed by calculation of the colony area and perimeter using in-built functions in Fiji-ImageJ. Using this, we calculate a parameter termed the shape factor, defined herein as the ratio between the perimeter and the square root of the area (for a circle, the shape factor equals 3.54). This quantity gives an estimate of how much colony shapes differ across various species and treatment conditions.

4.6. DNA Extraction and qPCR

For genetic analysis of 3D media-grown and liquid (t0, initial inoculum) co-culture samples, we carry out genomic DNA extraction. 300 μl of each sample is incubated at 65°C for 2 hrs with 200 μl of Promega nuclei lysis buffer, followed by the addition of 200 μl Promega protein precipitation solution and 100 μl of chloroform to promote phase separation. The DNA-containing fraction is separated out by centrifugation, to which 300 μl isopropyl alcohol is added to precipitate the nucleic acids fraction. The resultant pellet is washed twice with 80% ethanol, following which we elute the genomic DNA in 40μL nuclease-free water. To determine the change in the relative proportion of the two co-cultured strains, we amplify the V3-V4 hypervariable region of the bacterial 16S rRNA gene using the modified Illumina 10N primer [46] and sequence amplicons on the Illumina Miseq platform (300x2 paired-end, obtaining ~~75000-140000 reads per sample). We analyze sequence data using the DADA2 pipeline [47] in R, which gives us the relative abundance of each strain in each sample.

4.7. Simulating bacterial growth

We simulate 3D colony growth using a previously published agent-based platform (CellModeller[28]) which models bacterial cells as spherocylinders. We modify the original code by altering the aspect ratio of these objects by explicitly defining the radius and overall volume, which together adjust the cell's length. Using this, we simulate 3D growth of either high-aspect ratio "rods", or low-aspect ratio "spheres". We trigger the cells to divide once they achieve a target volume greater than twice the defined volume for a single cell, with both resultant daughter cells starting off with the initial volume defined for a single cell. Further, we constrain the progeny cells produced by rods to maintain orientation along the parental axis, whereas the progeny cells produced by spherical cells are allowed to reorient in random directions. We also simulate different degrees of physical confinement by varying the environmental drag (Γ) on the growing bacterial cells.

4.6. Statistical analysis

For each strain of bacteria, we record the OD_{600} for a minimum of 4 sets of biological replicates in both low confinement and high confinements matrices. Each set of biological replicates for each type of matrix contains OD_{600} data from 2 to 4 technical replicates. For simplicity, consider the data from high confinement to have a mean A_{high} and standard deviation dA_{high}, while for low confinement this would be A_{low} and dA_{low}, respectively. This can be considered as two random variables A_{high} and A_{low}, with errors of dA_{high} and dA_{low}, respectively. Now, the relative biomass ratio (ρ) can be written as:

$$\rho = A_{high} / A_{low}$$

where $d\rho$ is the propagated error from the technical replicates of both A_{high} and A_{low}. This can be formulated as:

$$d\rho = \sqrt{\left(\left(\frac{\partial \rho}{\partial A_{high}}\right) dA_{high}\right)^2 + \left(\left(\frac{\partial \rho}{\partial A_{low}}\right) dA_{low}\right)^2}$$

Now, $\frac{\partial \rho}{\partial A_{high}} = \frac{1}{A_{low}}$ and $\frac{\partial \rho}{\partial A_{low}} = -\frac{A_{high}}{{A_{low}}^2}$, hence, we get:

$$d\rho = \sqrt{\left(\left(\frac{1}{A_{low}}\right) dA_{hig}\right)^2 + \left(\left(-\frac{A_{high}}{{A_{low}}^2}\right) dA_{low}\right)^2}$$

Multiplying and dividing R.H.S. by ρ, we get:

$$d\rho = \rho * \sqrt{\left(\frac{dA_{high}}{A_{high}}\right)^2 + \left(\frac{dA_{low}}{A_{low}}\right)^2}$$

Hence, $\rho = A_{high} \Big/ A_{low} \pm \rho * \sqrt{\left(\frac{dA_{high}}{A_{high}}\right)^2 + \left(\frac{dA_{low}}{A_{low}}\right)^2}$

Now, consider the relative biomass ratios of any n such biological replicates, i.e., some ρ_1, ρ_2, … ρ_3, from n independent experiments. The average of these will be given by:

$$\rho_{avg} = (\rho_1 + \rho_2 + \ldots + \rho_n) \,/\, n$$

where, $d\rho_{avg}$ should represent the propagated error from all the individual relative biomass ratio values. This can be represented as:

$$d\rho_{avg} = \sqrt{\left(\left(\frac{\partial \rho_{avg}}{\partial \rho_1}\right) d\rho_1\right)^2 + \left(\left(\frac{\partial \rho_{avg}}{\partial \rho_2}\right) d\rho_2\right)^2 + \ldots + \left(\left(\frac{\partial \rho_{avg}}{\partial \rho_n}\right) d\rho_n\right)^2}$$

Herein, we know that $\frac{\partial \rho_{avg}}{\partial \rho_1} = \frac{\partial \rho_{avg}}{\partial \rho_2} = \frac{\partial \rho_{avg}}{\partial \rho_n} = \frac{1}{n}$, which reduces the above to:

$$d\rho_{avg} = \sqrt{(d\rho_1)^2 + (d\rho_2)^2 + \ldots + (d\rho_n)^2} \,/\, n$$

Hence, the net relative biomass ratio for n biological replicates, each with its own technical replicates, will be given by:

$$\rho_{avg} = (\rho_1 + \rho_2 + \rho_3 + \ldots + \rho_n) \,/\, n \pm \sqrt{(d\rho_1)^2 + (d\rho_2)^2 + (d\rho_3)^2 + \ldots + (d\rho_n)^2} \,/\, n$$

References

1. Leff, J. W. *et al.* Consistent responses of soil microbial communities to elevated nutrient inputs in grasslands across the globe. *Proc Natl Acad Sci U S A* **112**, 10967–10972 (2015).
2. Estrela, S., Sanchez-Gorostiaga, A., Vila, J. C. C. & Sanchez, A. Nutrient dominance governs the assembly of microbial communities in mixed nutrient environments. *Elife* **10**, (2021).
3. Keegstra, J. M., Carrara, F. & Stocker, R. The ecological roles of bacterial chemotaxis. *Nature Reviews Microbiology 2022 20:8* **20**, 491–504 (2022).
4. Gonzalez, D. & Mavridou, D. A. I. Making the Best of Aggression: The Many Dimensions of Bacterial Toxin Regulation. *Trends Microbiol* **27**, 897–905 (2019).
5. Blasche, S. *et al.* Metabolic cooperation and spatiotemporal niche partitioning in a kefir microbial community. *Nature Microbiology 2021 6:2* **6**, 196–208 (2021).
6. Chang, C. Y., Bajić, D., Vila, J. C. C., Estrela, S. & Sanchez, A. Emergent coexistence in multispecies microbial communities. *Science (1979)* **381**, 343–348 (2023).
7. Persat, A. *et al.* The Mechanical World of Bacteria. *Cell* **161**, 988 (2015).
8. Datta, S. S., Steinberga, A. P. & Ismagilova, R. F. Polymers in the gut compress the colonic mucus hydrogel. *Proc Natl Acad Sci U S A* **113**, 7041–7046 (2016).
9. Ribet, D. & Cossart, P. How bacterial pathogens colonize their hosts and invade deeper tissues. *Microbes Infect* **17**, 173–183 (2015).
10. Gomez, S. *et al.* Substrate stiffness impacts early biofilm formation by modulating Pseudomonas aeruginosa twitching motility. *Elife* **12**, (2023).
11. Tchoufag, J., Ghosh, P., Pogue, C. B., Nan, B. & Mandadapu, K. K. Mechanisms for bacterial gliding motility on soft substrates. *Proc Natl Acad Sci U S A* **116**, 25087–25096 (2019).
12. Flemming, H. C. *et al.* Biofilms: an emergent form of bacterial life. *Nature Reviews Microbiology 2016 14:9* **14**, 563–575 (2016).
13. Schloss, P. D. & Handelsman, J. Toward a Census of Bacteria in Soil. *PLoS Comput Biol* **2**, e92 (2006).
14. Fan, Y. & Pedersen, O. Gut microbiota in human metabolic health and disease. *Nature Reviews Microbiology 2020 19:1* **19**, 55–71 (2020).
15. Nicholson, P. G. *Soil Improvement and Ground Modification Methods*. *Soil Improvement and Ground Modification Methods* (2015).
16. Lu, P., Takai, K., Weaver, V. M. & Werb, Z. Extracellular matrix degradation and remodeling in development and disease. *Cold Spring Harb Perspect Biol* **3**, (2011).
17. Belkaid, Y. & Hand, T. W. Role of the microbiota in immunity and inflammation. *Cell* **157**, 121–141 (2014).
18. Kreda, S. M., Davis, C. W. & Rose, M. C. CFTR, Mucins, and Mucus Obstruction in Cystic Fibrosis. *Cold Spring Harb Perspect Med* **2**, a009589 (2012).

19. Shao, X. *et al.* Growth of bacteria in 3-d colonies. *PLoS Comput Biol* **13**, e1005679 (2017).
20. Martinez-Calvo, A. *et al.* Morphological instability and roughening of growing 3D bacterial colonies. *Proc Natl Acad Sci U S A* **119**, e2208019119 (2022).
21. Dell'Arciprete, D. *et al.* A growing bacterial colony in two dimensions as an active nematic. *Nature Communications 2018 9:1* **9**, 1–9 (2018).
22. You, Z., Pearce, D. J. G., Sengupta, A. & Giomi, L. Mono-to Multilayer Transition in Growing Bacterial Colonies. *Phys Rev Lett* **123**, 178001 (2019).
23. Bhattacharjee, T. & Datta, S. S. Bacterial hopping and trapping in porous media. *Nature Communications 2019 10:1* **10**, 1–9 (2019).
24. Lai, S. K., Wang, Y. Y., Hida, K., Cone, R. & Hanes, J. Nanoparticles reveal that human cervicovaginal mucus is riddled with pores larger than viruses. *Proc Natl Acad Sci U S A* **107**, 598–603 (2010).
25. Sardelli, L. *et al.* Towards bioinspired in vitro models of intestinal mucus. *RSC Adv* **9**, 15887–15899 (2019).
26. Kamashev, D., Balandina, A. & Rouviere-Yaniv, J. The binding motif recognized by HU on both nicked and cruciform DNA. *EMBO J* **18**, 5434–5444 (1999).
27. Burby, P. E. & Simmons, L. A. Regulation of cell division in bacteria by monitoring genome integrity and DNA replication status. *J Bacteriol* **202**, (2020).
28. Rudge, T. J., Steiner, P. J., Phillips, A. & Haseloff, J. Computational Modeling of Synthetic Microbial Biofilms. *ACS Synth Biol* **1**, 345–352 (2012).
29. Pinho, M. G., Kjos, M. & Veening, J. W. How to get (a)round: mechanisms controlling growth and division of coccoid bacteria. *Nature Reviews Microbiology 2013 11:9* **11**, 601–614 (2013).
30. Bean, G. J. *et al.* A22 disrupts the bacterial actin cytoskeleton by directly binding and inducing a low-affinity state in MreB. *Biochemistry* **48**, 4852–4857 (2009).
31. Khandige, S. *et al.* DamX controls reversible cell morphology switching in uropathogenic escherichia coli. *mBio* **7**, 642–658 (2016).
32. McGinnis, J. M. *et al.* Paracoccus sanguinis sp. nov., isolated from clinical specimens of New York state patients. *Int J Syst Evol Microbiol* **65**, 1877–1882 (2015).
33. Nokhal, T. H. & Mayer, F. Structural analysis of four strains of Paracoccus denitrificans. *Antonie Van Leeuwenhoek* **45**, 185–197 (1979).
34. Quinn, R. A. *et al.* Niche partitioning of a pathogenic microbiome driven by chemical gradients. *Sci Adv* **4**, (2018).
35. Baran, R. *et al.* Exometabolite niche partitioning among sympatric soil bacteria. *Nature Communications 2015 6:1* **6**, 1–9 (2015).
36. Brochet, S. *et al.* Niche partitioning facilitates coexistence of closely related gut bacteria. *Elife* **10**, (2021).
37. Nair, R. R. *et al.* Bacterial predator-prey coevolution accelerates genome evolution and selects on virulence-associated prey defences. *Nature Communications 2019 10:1* **10**, 1–10 (2019).
38. Wongkiew, S., Chaikaew, P., Takrattanasaran, N. & Khamkajorn, T. Evaluation of nutrient characteristics and bacterial community in agricultural soil groups for sustainable land management. *Scientific Reports 2022 12:1* **12**, 1–13 (2022).

39. Battesti, A., Majdalani, N. & Gottesman, S. The RpoS-mediated general stress response in escherichia coli *. *Annu Rev Microbiol* **65**, 189–213 (2011).
40. Benomar, S. *et al.* Nutritional stress induces exchange of cell material and energetic coupling between bacterial species. *Nature Communications 2015 6:1* **6**, 1–10 (2015).
41. Peterson, S. B., Bertolli, S. K. & Mougous, J. D. Interbacterial antagonism: at the center of bacterial life. *Curr Biol* **30**, R1203 (2020).
42. MacLean, R. C., Torres-Barceló, C. & Moxon, R. Evaluating evolutionary models of stress-induced mutagenesis in bacteria. *Nature Reviews Genetics 2013 14:3* **14**, 221–227 (2013).
43. Foster, P. L. Stress-Induced Mutagenesis in Bacteria. *Crit Rev Biochem Mol Biol* **42**, 373 (2007).
44. Tran, T. D., Ali, M. A., Lee, D., Félix, M. A. & Luallen, R. J. Bacterial filamentation as a mechanism for cell-to-cell spread within an animal host. *Nature Communications 2022 13:1* **13**, 1–11 (2022).
45. Crocker, J. C. & Grier, D. G. Methods of Digital Video Microscopy for Colloidal Studies. *J Colloid Interface Sci* **179**, 298–310 (1996).
46. Naik, T., Sharda, M., Lakshminarayanan, C. P., Virbhadra, K. & Pandit, A. High-quality single amplicon sequencing method for illumina MiSeq platform using pool of 'N' (0-10) spacer-linked target specific primers without PhiX spike-in. *BMC Genomics* **24**, (2023).
47. Callahan, B. J. *et al.* DADA2: High-resolution sample inference from Illumina amplicon data. *Nature Methods 2016 13:7* **13**, 581–583 (2016).

Acknowledgments

T.B. and D.A. acknowledge intramural research grants from NCBS (Department of Atomic Energy Project 695 Identification No. RTI 4006). D.A. acknowledges a grant from the DBT/Wellcome Trust India Alliance (IA/I/17/1/503091) that also supported P.S. M.S. acknowledges personal support through the NCBS GS program. M.S. also acknowledges help from Saheli Dey, Kiruthika Kumar, and Manukrishna Manikandan for training on handling bacterial cultures and preparation of 3D growth media. We are grateful to Dr. Anjana Badrinarayan for kindly sharing the DNA damage-reporting *E. coli* strains. We also acknowledge the helpful inputs from Dr. Tim Rudge on computational simulations of bacterial growth. We thank Dr. Sneha Garge, Krithjgnan Bhardwaj, and Dhanush A for isolating bacterial strains from the flour beetle gut. We are grateful to Dr. H. Krishnamurthy and the Central Imaging and Flow Cytometry Facility, and the NGS facility at NCBS. We also acknowledge the NCBS common equipment facility for arranging the Varioskan multimode plate reader and the Anton Parr MCR 302e rheometer.

Author contributions

T.B. conceptualized and supervised the study. T.B., M.S., D.A., and P.S. contributed towards the study design. M.S. performed the experiments, simulations, and data analysis, with help from M.G. P.S. characterized the gut-derived microbial strains and performed the genetic analysis. C.K. helped with the computational simulations setup. M.S. and T.B. wrote the manuscript with help from D.A. and C.K. T.B. acquired primary funding support. All authors provided critical feedback on the manuscript.

Competing interest

The authors declare no competing interest.

Correspondence and requests for materials should be addressed to Tapomoy Bhattacharjee (tapa@ncbs.res.in).

Supplementary data

Physical confinement selectively favours bacterial growth based on cell shape

M Sreepadmanabh[1], Meenakshi Ganesh[1,2], Pratibha Sanjenbam[1], Christina Kurzthaler[3], Deepa Agashe[1], and Tapomoy Bhattacharjee[1*]

[1]National Centre for Biological Sciences, Tata Institute of Fundamental Research, Bangalore
[2]Indian Institute of Science Education and Research, Mohali
[3]Max Planck Institute for the Physics of Complex Systems, Dresden
*email: tapa@ncbs.res.in

Supplementary data figures

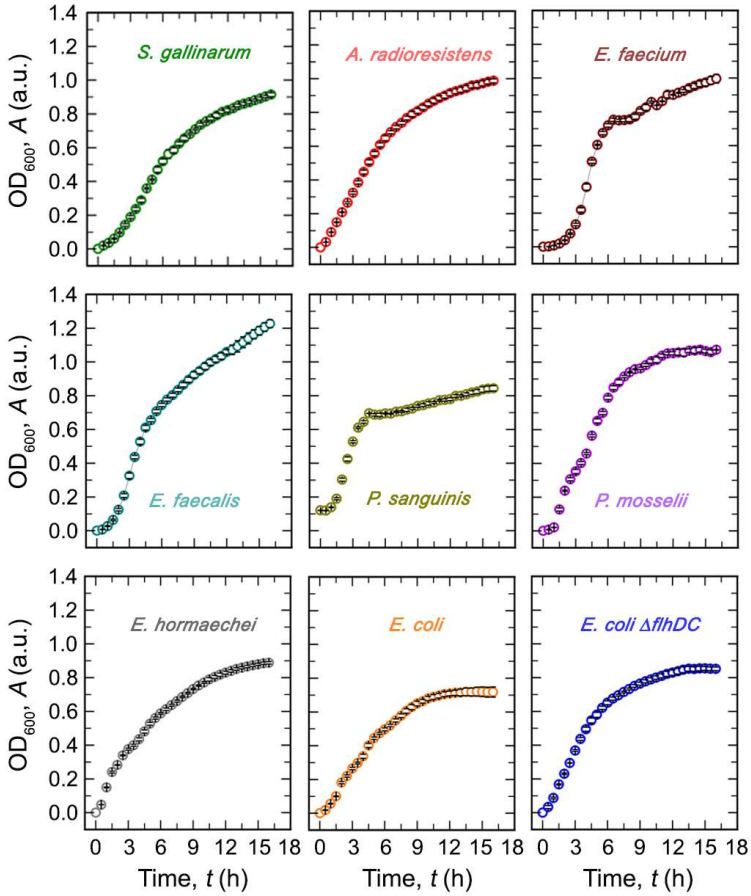

Supplementary data Figure 1: Absorbance-based growth curves for all bacterial strains in LB broth under continuously shaken culturing conditions (from 3 technical replicates).

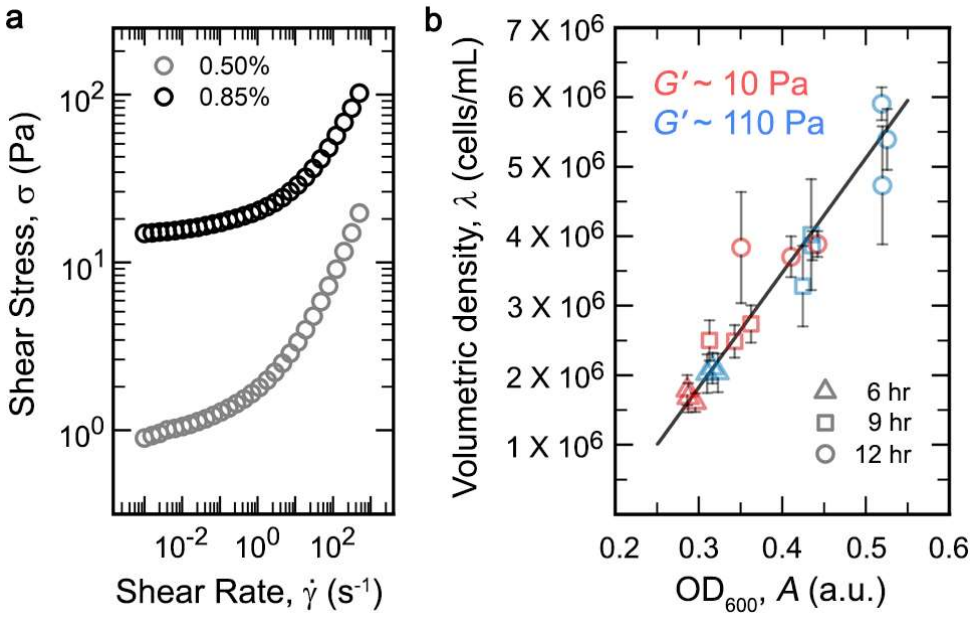

Supplementary data Figure 2: (a) Rheological measurements reveal that the 3D growth media behaves as a yield stress material – i.e., it undergoes reversible fluidization at high shear rates while behaving as a soft solid at low shear rates. (b) A comparison between absorbance measurements and volumetric density of cells shows a broadly linear relation for both the low confinement and high confinement matrices, indicating that the optical density-based absorbance measurements can be used as a reliable indicator of total bacterial biomass for the 3D growth media. Volumetric density is measured by manually counting the total number of cells present in a 3D volumetric image from confocal microscopy.

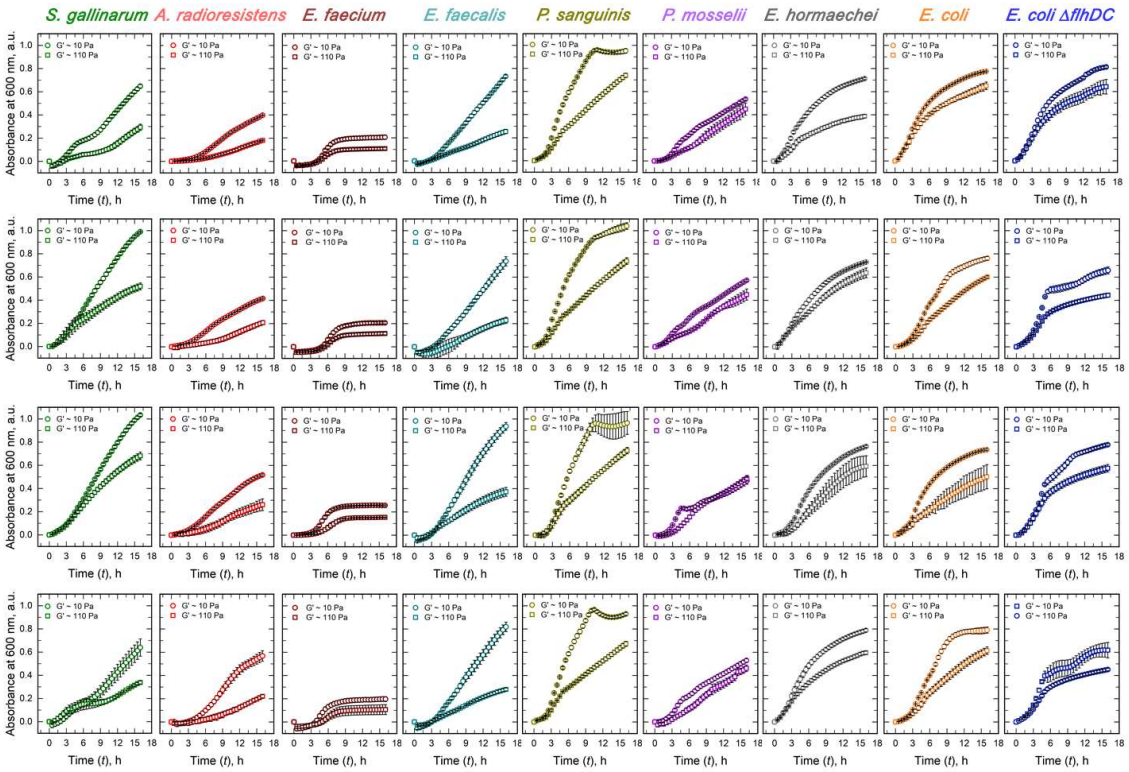

Supplementary data Figure 3: Representative biological replicates from growth curve assays in 3D microgel growth media for all bacterial strains used in this study.

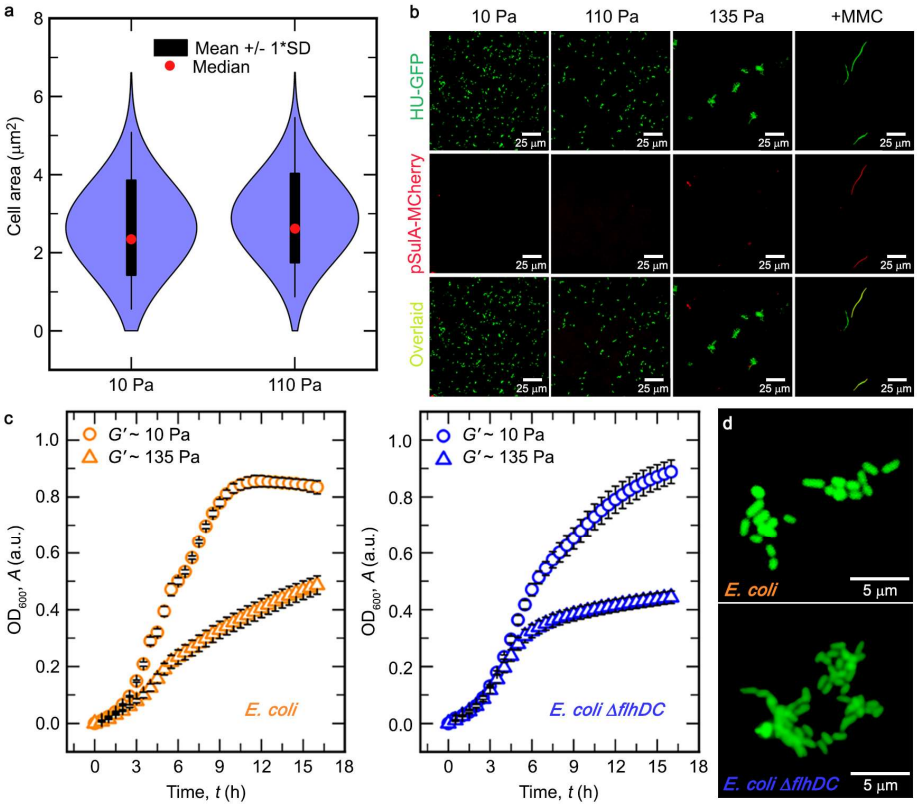

Supplementary data Figure 4: (a) The degree of physical confinement within jammed microgel growth media does not alter the cellular morphology of bacterial cells, as shown here for non-motile *E. coli* cells. (b) Growth under confinement does not affect the genomic integrity of bacteria, as evidenced by the lack of DNA damage response reporter (SulA, tagged to MCherry) expression. The Hu-GFP reporter is tagged to a histone protein that localizes with genomic DNA. (c) Motility does not confer significantly greater growth benefits under confinement. Using highly confined microgel growth media, we observe that both motile and non-motile *E. coli* perform similarly. (d) Under such high degrees of confinement (G' ~ 135 Pa microgels) both motile and non-motile *E. coli* form elongated colonies.

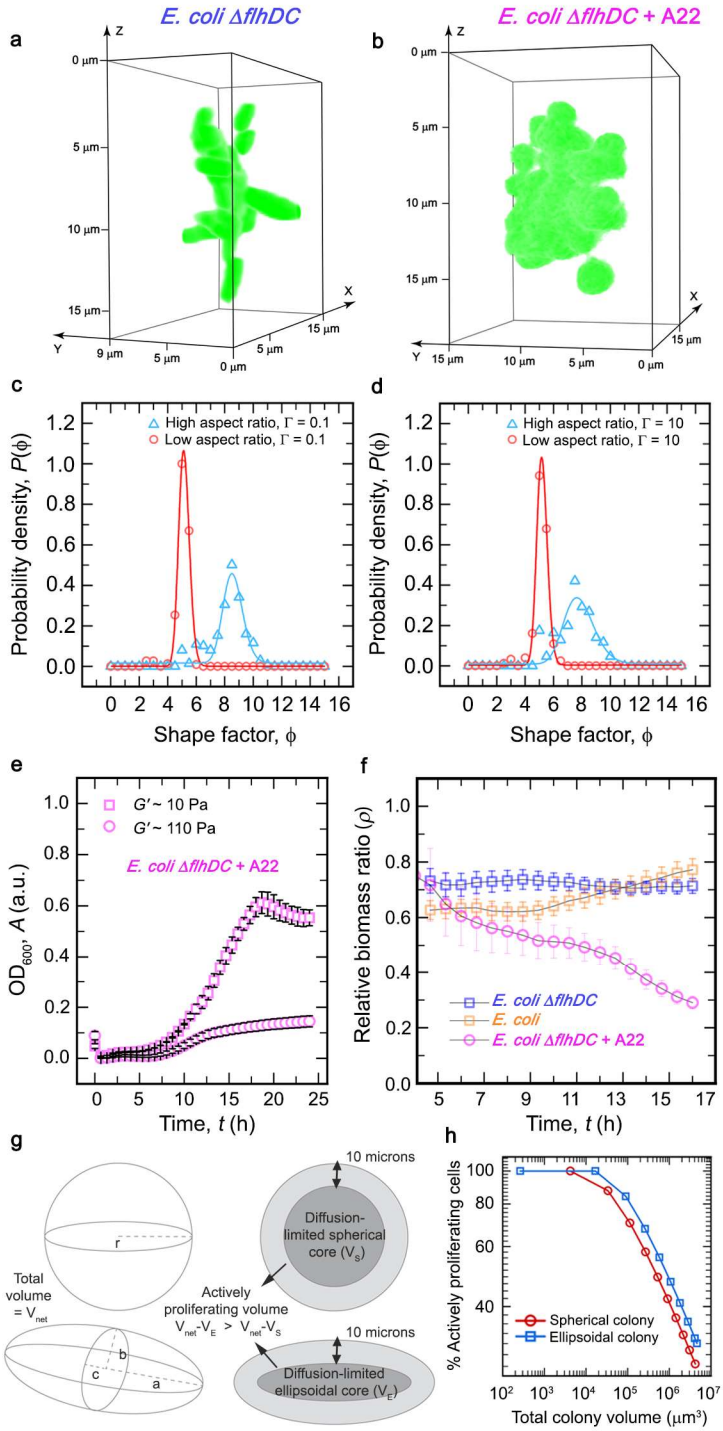

Supplementary data Figure 5: (a and b) 3D reconstructions of colonies formed by rod-shaped and approximately spherical *E. coli* during growth in the high confinement matrix. (c and d) Quantitative analysis of colony morphologies using the shape factor metric, generated using simulations with different conditions of environmental drag (Γ) on bacterial growth. In all cases, a clear distinction is visible between colonies formed by high vs. low aspect ratio bacteria, with the former organizing into colonies with a high shape factor value (more elongated), whereas, the latter organizes into more rounded colonies with a low shape factor

value. (e) Representative growth curves of *E. coli* treated with A22 under two different degrees of confinement, assayed for twenty-four hours of growth, considering the antibiotic-induced delay in proliferation. (f) Relative biomass ratio (ρ) across sixteen hours of growth under confinement for *E. coli*, non-motile *E. coli*, and non-motile *E. coli* treated with A22, showing how a shift in the bacterial shape towards approximately spherical morphology dramatically diminishes the relative growth success under increased confinement. (g) Schematic representations of numerical calculations considering either spherical colonies formed by low aspect ratio (=1) cells or ellipsoidal colonies formed by high aspect ratio (=4) cells. From previous work on *E. coli* confined in 3D porous media, we assume a maximum depth of ~10 μm up to which nutrient diffusion allows active proliferation of cells, beyond which the colony's core remains nutrient limited and hence metabolically inactive. (h) The proportion of actively proliferating cells in colonies of different sizes for either condition, showing that ellipsoidal colonies formed by high aspect ratio cells retain a significantly higher proportion of cells in the actively proliferating fraction, compared to spherical colonies formed by low aspect ratio cells, for colonies of comparable sizes.

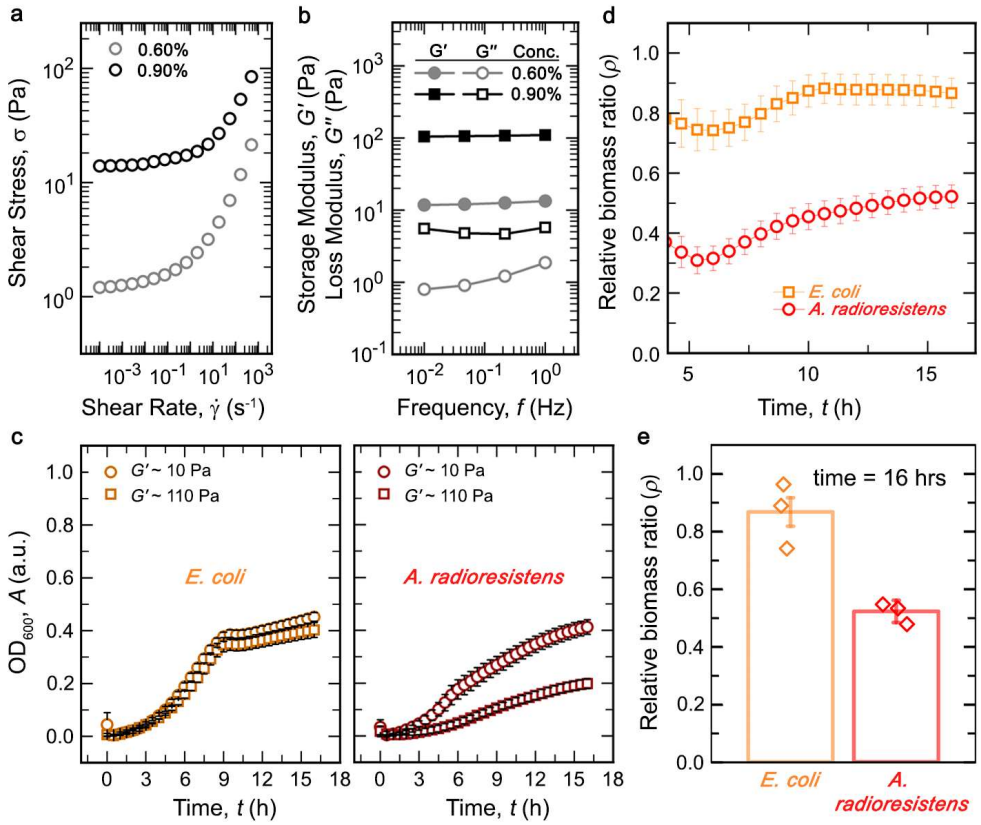

Supplementary data Figure 6: Characterizing bacterial growth dynamics in minimal media (M9)-based jammed microgel matrix. We replicate conditions of confinement similar to those imposed by the LB-based microgels using M9-based 3D growth matrix. (a and b) Rheological characterization of M9-based microgels reveals physical properties matching that of LB-based 3D growth media. (c) To test whether the trends exhibited by relative biomass ratios for low and high aspect bacteria are independent of nutrient composition, we assay the high aspect ratio *E. coli* and low aspect ratio *A. radioresistens* in minimal media (M9) supplemented with 0.2% glucose and 0.2% milk protein hydrolysate. (d and e) Relative biomass ratio trends over 16 hours of growth for the rod-shaped *E. coli* and spherical *A. radioresistens* across two different degrees of confinement using M9-based jammed microgel growth matrix. The results recapitulate what has been observed using LB-based 3D growth matrix, with the high aspect ratio *E. coli* exhibiting a superior relative biomass ratio under a higher degree of confinement.

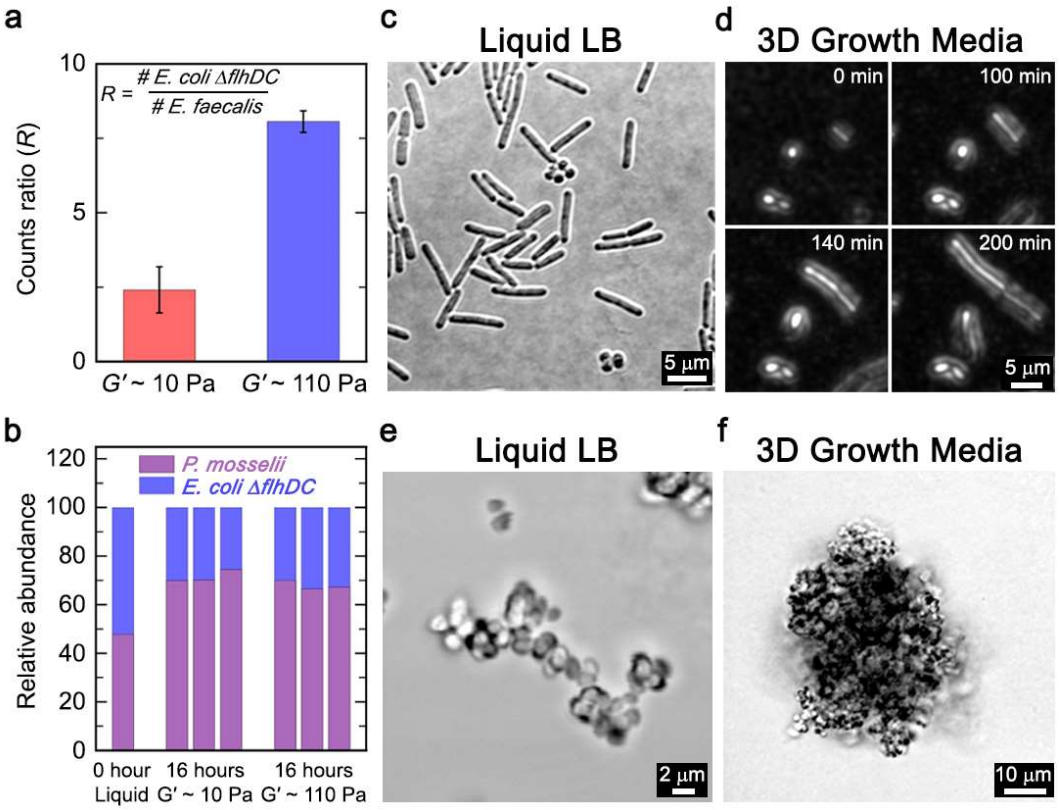

Supplementary data Figure 7: (a) 3D co-culture models show that high aspect ratio cells (non-motile *E. coli*) enjoy a distinct advantage over low aspect ratio cells (*E. faecalis*) upon an increase in physical confinement, wherein the relative abundance of the former is significantly enriched starting from initial inoculums with comparable proportions of either. Here, we show data from the manual counting of single cells using confocal microscopy. (b) Using sequencing-based bulk genomic analysis, we show that between two high aspect ratio cells (*P. mosselii* and non-motile *E. coli*), neither enjoy a dramatic advantage upon a change in the degree of confinement – rather, their relative proportions stay largely similar across both matrices. (c and d) Growth under confinement leads to dramatically altered outcomes at both the colony and single-cell levels. *P. sanguinis* shows a mixed spherical and rod-shaped morphology in liquid LB, but within microgel growth media, exhibits highly filamentous growth, resulting in elongated colonies. (e and f) *E. faecalis*, which exhibits growth as elongated clusters in liquid LB, instead shows colony growth in the form of spherical colonies in the 3D growth media under physical confinement.

Supplementary data movies

Supplementary data Movie 1: Simulations of bacterial colony growth in 3D.

Supplementary data Movie 2: Microscopic imaging of bacterial colony growth inside 3D matrices.